Multifidelity Multipoint Proprotor Blade Optimization for Urban Air Mobility

Christopher S. Thurman
christopher.thurman@nasa.gov
Aeroacoustics Branch
NASA Langley Research Center
Hampton, VA, USA

Li Wang
li.wang@nasa.gov
Computational Aerosciences Branch
NASA Langley Research Center
Hampton, VA, USA

ABSTRACT

A multifidelity, multipoint aerodynamic blade shape optimization was conducted to design a realistic, full-sized proprotor, representative of recent industry tiltrotor and lift+cruise UAM vehicle designs. The proprotor was designed to achieve a disk loading of 8 psf in hover at sea level standard day and 1.9 psf in cruise at an altitude of 4000 ft above ground level with a multipoint efficiency optimization target. A low-fidelity optimization was first conducted using a differential evolution algorithm with CAMRAD II's uniform inflow model, followed by a mid-fidelity trim using CAMRAD II's nonuniform inflow and free-wake models, a high-fidelity verification using a hybrid RANS/LES approach in FUN3D, and finally a high-fidelity optimization on the low-fidelity optimized blade shape with a gradient-based method using a uRANS approach in FUN3D. The low-fidelity optimization resulted in a proprotor that achieved a hover figure of merit of 0.830 and a propulsive efficiency in cruise of 0.904. Results from the low-fidelity optimization, mid-fidelity trim, and high-fidelity verification were compared to highlight differences in predicted blade span loading and aerodynamic efficiency between the different aerodynamic solvers. It was shown that the low-fidelity solver compared least favorably with the high-fidelity aerodynamic solver. Lastly, the high-fidelity optimization further reduced the torque in cruise by approximately 75 ft-lb, with negligible changes in hover figure of merit and propulsive efficiency in cruise. Negligible blade shape differences were observed between the low-fidelity optimized design and the results from the sequential high-fidelity optimization with the largest difference being collective pitch in both hover and cruise, respectively.

NOMENCLATURE

$c(r)$	Rotor chord length distribution, ft
DL	Rotor disk loading, lb/ft
FM	Rotor figure of merit
J	Propeller advance ratio
M_{tip}	Mach number at the rotor blade tip
M_∞	Freestream Mach number
N_b	Number of rotor blades
Q	Rotor generated torque, ft-lb
r	Normalized span location, $\frac{x}{R}$
R	Rotor radius, ft
T	Rotor generated thrust, lb
w_c	Cost function weight for cruise efficiency
w_h	Cost function weight for hover efficiency
y^+	Normalized wall distance
α	Angle of attack, deg
$\Delta\psi$	Flow solver time step, deg
$\theta_{tw}(r)$	Rotor twist distribution, deg
θ_0	Rotor collective pitch measured at root, deg
κ	UMUSCL dissipation tuning parameter
η	Propeller efficiency
Ω	Rotor rotational rate, revolutions per minute (RPM)

Presented at the Vertical Flight Society's 81st Annual Forum & Technology Display, Virginia Beach, VA, May 20–22, 2025.

INTRODUCTION

Advanced Air Mobility (AAM) has seen growing interest over the past decade by government, industry, and academia. AAM vehicles typically utilize multirotor systems for lift and/or propulsion, which can often be unconventional and may incorporate collective pitch, rotor speed, rotor shaft tilt angle, or combinations of these controls to support operational conditions ranging from vertical takeoff/landing (VTOL), through transitional modes, to cruise, or axial forward flight with the rotor plane(s) orthogonal to the oncoming flow. Since these AAM rotors typically don't entail cyclic pitch control, they are often referred to as proprotors. The flexibility of these AAM vehicles make them exceptional candidates for missions involving the transportation of cargo and personnel, with the latter being the target for Urban Air Mobility (UAM). UAM, as defined by the NASA white paper on UAM Noise, is a "rapidly emerging market requiring high density VTOL operations for on demand, affordable, quiet, fast, transportation in a scalable and conveniently accessible verti-port network" (Ref. 1).

To date, many concept and production UAM vehicles exist, and Ref. 2 provides a comprehensive list of all known electric and hybrid-electric VTOL vehicles. The Revolutionary Vertical Lift Technology (RVLT) Project at NASA has also provided conceptual vehicle designs, such as the tiltwing (Ref. 3) and lift+cruise (Ref. 4) reference configurations, among others, to serve as research testing platforms. Though these reference vehicles bear similarity to preproduction vehicles designed by industry in terms of mission requirements, the proprotors for these RVLT conceptual vehicles are often notional or canonically designed using analytical expressions (Ref. 3) and low-fidelity tools (Ref. 5). Additionally, more realistic proprotors for UAM operation like those on preproduction vehicles are often proprietary and not accessible to the public, with few exceptions (e.g., prototype proprotor from Joby Aviation (Refs. 6, 7) and a hover-optimized proprotor designed by Techsburg, Inc. (Ref. 8)). Moreover, much of the UAM proprotor noise facility testing and computations performed by NASA have focused on small Unmanned Aerial Systems (sUAS), or drone-sized proprotors (Refs. 9–12) due to this limitation of representative UAM proprotor geometries in addition to facility limitations (e.g., facility size and testing cost).

The goal of this work is to design a realistic and representative full-scale UAM proprotor to serve as a benchmark research platform for aerodynamic and acoustic studies with the intent of coordinating UAM noise research efforts. UAM mission requirements outlined in Whiteside et al. (Ref. 3) will be used to define the operating conditions for design, with a modified hover condition thought to be more representative of current industry designs (i.e., tiltrotor and lift+cruise). A multipoint optimization will be performed to design the proprotor at two operating points, namely, hover and cruise at altitude. Single-point, low-fidelity optimizations have previously been conducted by NASA for UAM cruise conditions (Ref. 13); however, a major drawback of the low-fidelity tools often used for proprotor optimization is that they may not account for salient flow features necessary for accurate proprotor performance and acoustic prediction. To circumvent this issue, an approach similar to the work performed by Abergo, et al. (Ref. 14) will be used where the proprotor will first be optimized using low-fidelity methods followed by a successive high-fidelity optimization. In this fashion, flow physics will be incrementally injected into the design problem, ensuring adequate resolution of realistic flow features (i.e., cross-flow, compressibility, and tip vortex effects) during the optimization procedure.

TECHNICAL APPROACH

A multifidelity optimization was used in this work that consisted of two separate but sequential optimizations. The first optimization utilized a low-fidelity aerodynamic solver within a genetic algorithm optimization framework and will be discussed in the Low-Fidelity Optimization subsection. Since the low-fidelity aerodynamic solver relies on analytical and empirical modeling, it is capable of producing quick results at the expense of not accounting for all relevant flow physics. Quick results are very desirable for an optimization problem; however, the lack of aerodynamic fidelity has previously led to major differences between experimental data and low-fidelity predictions such as those caused by tip vortex-induced blade separation (Refs. 15,16). To circumvent potential issues caused by the lack of fidelity, a successive optimization was conducted using a high-fidelity unsteady Reynolds-averaged Navier-Stokes (uRANS) aerodynamic solver with the low-fidelity optimized design as the starting point. This high-fidelity optimization used a gradient-based methodology and will be discussed in the High-Fidelity Optimization subsection.

Prior to the high-fidelity optimization, the low-fidelity optimized proprotor was trimmed using mid-fidelity methods and slight alterations were made to the blade root for structural purposes. Then, this post-trim modified proprotor was verified using high-fidelity CFD. The trimming procedure, blade root alterations, and high-fidelity CFD verification will be discussed in the Trim and Verification Subsection. An illustration of the technical approach used in this work is shown in Fig. 1.

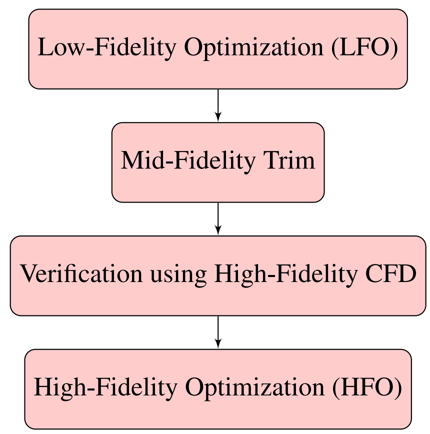

Figure 1: Block diagram representation of technical approach.

Design Requirements

The goal of this work was to optimize a proprotor blade geometry for operation at two conditions: hover at sea level standard day and cruise at an altitude of 10,000 ft ISA (i.e., 4000 ft above ground level). Both operating points were defined in Whiteside et al. (Ref. 3) for the RVLT tiltwing concept vehicle and are shown in Table 1; however, a hover disk loading, DL_h, of 8 psf was used in this work rather than the $DL_h = 20$ psf detailed in the reference. This lower DL_h was thought to be characteristic of tilting proprotor-type applications and more representative of recent tiltrotor and lift+cruise UAM vehicle designs such as the Joby Aviation S4 (Ref. 17), Archer Aviation Midnight (Ref. 18), and the Wisk Aero Generation 6 (Ref. 19). The proprotor has five blades (i.e., $N_b = 5$), and its size was held constant at a radius of $R = 3.61$ ft. The proprotor speed in hover was fixed at $\Omega_h = 886$ RPM ($M_{\text{tip}} = 0.3$) and in cruise, $\Omega_c = 725$ RPM ($M_{\text{tip}} = 0.2543$). Though the proprotor speed in cruise was dictated by the advance ratio of $J = 3.0$ and inflow speed of $M_\infty = 0.2428$ detailed in Ref. 3, acoustic tonal noise reduction was considered when prescribing the low value of Ω_h (Ref. 20).

The multipoint optimization objective for both the low- and high-fidelity optimization efforts in this work was to maximize hover figure of merit, FM, and cruise propulsive effi-

Table 1: Design operating points.

Operating Point	Altitude (ft)	Propeller Advance Ratio, J	Rotation Rate (RPM)	Disk Loading (psf)
Hover	0.0	0.0	886 ($M_{\text{tip}} = 0.3$)	8.0
Cruise	10,000	3.0 ($M_\infty = 0.2428$)	725 ($M_{\text{tip}} = 0.2543$)	1.9

ciency, η, subject to constraints on hover and cruise disk loading values of $DL_h = 8$ psf and $DL_c = 1.9$ psf, respectively.

Low-Fidelity Optimization

For the initial low-fidelity optimization (LFO) conducted in this work, the differential evolution algorithm of Storn and Price (Ref. 21) as implemented in the SciPy library (Ref. 22), was used. This optimization algorithm is a population-based stochastic process, which are known for converging to a global optimum rather than local optima. Starting with an initial Sobol sample space consisting of 28 points, a 'rand/1/bin' mutation strategy was used. The optimizer works by perturbing the initial sample space to generate new trial points, evaluating the cost function at these new trial points, and replacing points in the original sample space with these new trial points if there was a cost function improvement. This process was repeated over a maximum of 2000 iterations or until the change in cost function between two successive iterations fell below 0.0001.

The Comprehensive Analytical Model of Rotorcraft Aerodynamics and Dynamics (CAMRAD II) (Ref. 23) was used as the aerodynamic solver. CAMRAD II is a comprehensive rotorcraft analysis code allowing for the use of different wake models (e.g., uniform inflow, prescribed wake, and free-wake) and blade dynamics (e.g., rigid and elastic). CAMRAD II requires airfoil aerodynamic coefficient data, which can either be generated using analytical equations or can be supplied by the user in the form of an airfoil table.

CAMRAD II was used for the LFO with a uniform inflow model and no wake modeling, which significantly reduced computational cost associated with predictions at each design point. Based upon previous user experience with the NACA 6-series (Ref. 16) and inspiration from the XV-15 rotor design (Ref. 24), the NACA 64A412 was selected as the airfoil geometry used along the blade span for the low-fidelity portion of this work and was not modified throughout the optimization procedure. Airfoil tables in the C81 format were generated for the NACA 64A412 using the structured uRANS solver, OVERFLOW2 (Ref. 25). Two-dimensional, steady-state OVERFLOW2 simulations were conducted over a range of angles of attack, α, and freestream Mach numbers, M_∞, using the improved Einfeldt's second-order spatial Harten, Lax, and van Leer (HLLE++) upwind scheme (Ref. 26) and the one-equation Spalart-Allmaras turbulence model with rotation/curvature correction (SA-neg-noft2-RC). Values of α ranged from $-18^\circ \leq \alpha \leq +18^\circ$, and M_∞ values ranged from $0.1 \leq M_\infty \leq 0.6$. A chord-based reference Reynolds number, Re_{ref}, of four million was prescribed at $M_\infty = 1$, which was scaled by the M_∞ value correspondent to each simulation. This value for Re_{ref} was calculated using the average of the minimum and maximum chord length optimization constraints in Table 3. A preexisting C81 table generated for an NACA 0012 airfoil profile was used as a template and cubic interpolation was utilized to combine the airfoil coefficient data calculated using OVERFLOW2 with the preexisting template over the specified range of α and M_∞. It should be noted that low-Re effects were not considered in this work and are not expected based on the full-scale size of the proprotor and operating conditions.

Both the hover and cruise operating conditions were evaluated at each optimizer iteration. As previously mentioned, the optimization objective was to maximize hover FM and cruise η with the constraints: $DL_h = 8$ psf and $DL_c = 1.9$ psf, respectively. The optimization cost function was reconstructed as a minimization problem consisting of a linear combination of the difference between FM and unity and η and unity, where unity is the value for perfect efficiency:

$$f_{\text{cost}} = min\{w_h(1 - FM) + w_c(1 - \eta)\} \tag{1}$$

where: $w_h = 1$ and $w_c = 1$ for this work. The collective pitches of the proprotor in hover and cruise, $\theta_{0,h}$ and $\theta_{0,c}$, respectively, were left as design target variables for the optimization. Additionally, the blade twist, θ_{tw}, and chord length, c, at five equidistant spanwise locations (i.e., control points) between $0.2R \leq x \leq R$ were targeted for design optimization. The root cutout of $0.2R$ was deemed acceptable for root shank lofting to allow for hub installation. Cubic splining was used between the five control points to ensure smooth distributions of θ_{tw} and c. An arbitrary chord length distribution showing the five control points and cubic spline is shown in Fig. 2. Additional constraints were imposed on the optimizer to en-

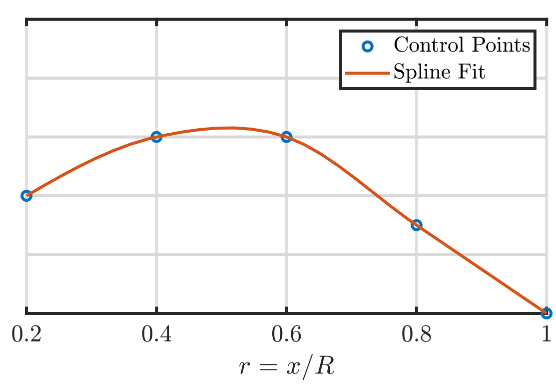

Figure 2: Representative chord length distribution.

sure the sectional angle of attack along the blade span, $\alpha(r)$, was above the zero-lift angle of attack and below stall for the NACA 64A412 airfoil. To ensure realistic designs, the twist and chord distributions were constrained to be decreasing outboard of $0.7R$ and to not have more than one slope change. The cost function and constraints are shown in Table 2, and the design variables (DVs) along with their minimum and maximum allowable values imposed on the optimizer are shown in Table 3.

Table 2: Cost function and constraints for low-fidelity optimization.

Cost Function	$min\{(1-FM)+(1-\eta)\}$
DL_h Constraint	$7.9\text{psf} \leq DL_h \leq 8.1$ psf
DL_c Constraint	$1.8\text{psf} \leq DL_c \leq 2.0$ psf
$\frac{d\theta_{tw}}{dr}(r > 0.7R)$	< 0
$\frac{dc}{dr}(r > 0.7R)$	< 0
$\alpha(r)$ Constraint	$-1.5^\circ \leq \alpha(r) \leq +12^\circ$

Table 3: Design variable ranges for low-fidelity optimization (1...5 denotes values at the five control points).

Design Variable	Minimum Value	Maximum Value
$\theta_{0,h}$	-15.0°	$+15.0^\circ$
$\theta_{0,c}$	0.0°	$+65.0^\circ$
$\theta_{tw,1...5}$	-25.0°	$+50.0^\circ$
$c_{1...5}$	0.328 ft	0.984 ft

Trim and Verification

Typically, uniform inflow results overpredict the thrust when compared to higher-fidelity methods. For this reason, after the LFO was conducted using CAMRAD II's uniform inflow model, the proprotor collective pitch was trimmed to the target disk loading values of $DL_h = 8$ psf and $DL_c = 1.9$ psf using CAMRAD II's free-wake solver. This free-wake solver can be considered a mid-fidelity method and, in general, is more accurate than the uniform inflow approach since more flow physics are resolved. This trimming procedure was performed to establish more accurate operating conditions to be used during the subsequent optimization so that very large collective pitch changes were not targeted by the high-fidelity optimizer.

CAMRAD II was used with a general free-wake geometry model consisting of a single-peak vortex defined by the magnitude of maximum blade circulation, a second-order trapezoidal distortion integration, a second-order lifting-line with a quarter chord collocation point, and a wake extent of ten rotor revolutions. Since the proprotor considered in this study did not have flap/lag hinges or pitch bearings, a potential source of structural vulnerability exists at the blade root. After trim was established, blade thickness was added to the proprotor for additional structural robustness by modifying the airfoil at $0.2R$ and $0.4R$ to an NACA 64A024 and NACA 64A414, respectively. Cubic splining was used to smoothly transition the different airfoil geometries along the blade span. A comparison of the thickness and camber distributions between the original and modified shape is shown in Fig. 3.

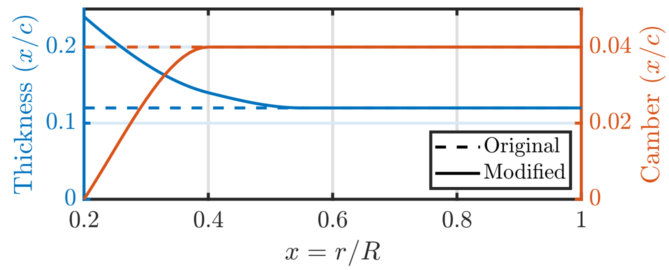

Figure 3: Thickness and camber comparison between original and structurally modified proprotor.

After the blade modification, fully unsteady proprotor simulations were conducted with the trimmed collective pitch values for both the hover and cruise operating conditions using the unstructured-grid uRANS code, FUN3D (Ref. 27). These simulations were performed to verify that the structural modifications had negligible impact on the aerodynamic performance and that the disk loading design criteria for both operating conditions were still satisfied. CFD grid and FUN3D solver details will be deferred to the next section; however, there are two distinctions between what was used for the high-fidelity optimization discussed and the verification simulations discussed here. The first difference is that volumetric cells in the wake resolution region were sized to be approximately 5% of the tip-chord length for the verification simulations as opposed to the 12% tip-chord length sizing for the high-fidelity optimizaton. The second difference is that a delayed detached eddy simulation (Ref. 28) was used for the verification simulations rather than solely using the one-equation Spalart-Allmaras (S-A) turbulence model (Ref. 29) for the high-fidelity optimization. Simulations of higher-fidelity were performed for the verification cases since computational cost was of less concern for these one-off simulations. A coarser volumetric spatial resolution was used for the high-fidelity optimization discussed in the next section because many simulations were performed during the optimization. Additionally, the FUN3D adjoint-based sensitivity analysis solver capability only supports the one-equation S-A turbulence model.

High-Fidelity Optimization

For the sequential high-fidelity optimization (HFO), a gradient-based method was implemented using the sequential quadratic-programming optimizer, SNOPT (Ref. 30) with FUN3D as the aerodynamic solver. Gradient-based design optimization relies on sensitivities of the cost function and constraints with respect to the design target variables. For this work, the adjoint of the uRANS flow solution was used to calculate these sensitivities. The sensitivities were then used along with the geometry parameterization tool, Multidisciplinary Aerodynamic-Structural Shape Optimization Using

Deformation (MASSOUD) software package (Ref. 31), to deform the surface grid, followed by a volumetric grid deformation using a generalized minimum residual method (Ref. 32) mesh elasticity solver. The optimization procedure is outlined in Fig. 4 and full details can be found in Wang et al. (Refs. 33,34). Since FUN3D accounts for aerodynamic effects such as cross-flow, compressibility, and tip vortices, this successive optimization can be thought of as a high-fidelity correction to the LFO.

The CFD grid used in this work was a composite overset mesh with separate component grids for each proprotor blade. These proprotor blade grids were immersed in a box-shaped background grid, which extended $50R$ away from the center of the proprotor. The separate blade grids contained 1,006,618 nodes, with 89,048 triangular surface elements and 5,941,954 volumetric tetrahedron elements. The background grid had 8,161,397 nodes or 50,537,368 volumetric tetrahedron elements. In total, the composite grid contained 13,194,487 nodes or 80,237,958 volumetric tetrahedron elements. A similar meshing strategy to that used by Thurman et al. (Ref. 35) was adopted in this work, including a wake resolution region extending approximately $3R$ below the proprotor, which is shown in Fig. 5. The cells in the wake resolution region were sized to be approximately 12% of the tip chord length. Additionally, the first volumetric cell adjacent to the blade was sized for a y^+ value less than unity.

FUN3D solver details have been provided by the authors in Ref. 35 and so will be excluded herein for brevity. It will, however, be noted that Roe's flux-difference splitting (Ref. 36) was used to calculate inviscid flux values together with primitive variable reconstruction using the second-order unstructured monotonic upstream scheme for conservation laws (UMUSCL) (Ref. 37) with $\kappa = 0.0$ (i.e., fully upwind). For the viscous terms of the RANS equations, the Green-Gauss theorem was used to compute cell-based gradients for a second-order approximation. A Boussinesq assumption related the Reynolds stress in the RANS equations to a mean strain-rate tensor and turbulent eddy viscosity determined using the one-equation S-A turbulence model. The Green-Gauss theorem was also used to compute a second-order approximation to the turbulence model diffusion terms. A dual-time approach was used to temporally advance the uRANS equations where point-implicit multicolor Gauss-Siedel iterations were executed at each time step to sufficiently reduce the residuals of the nonlinear system of equations. An optimized second-order backward differencing scheme (Ref. 38) was used for the time integration with a physical timestep correspondent to $\Delta\psi = 1^\circ$ of azimuthal advancement, or 360 steps per rotor revolution. Overset grid connectivity and communication was performed using the DiRTlib and SUGGAR++ software packages (Ref. 39).

After the forward-in-time flow solve, a discretely consistent adjoint-based sensitivity analysis was performed in FUN3D (Ref. 40) to calculate sensitivities of the cost function and constraints with respect to the DVs. For this work, various planform and shear DVs were initially included in the optimization; however, their inclusion caused unrealizable blade deformations that crashed the optimizer. Because of this, only collective, twist, camber, and thickness DVs were included in the HFO and are shown in Fig. 6. It should be noted that the camber and thickness DVs were not used for the LFO and that 11 spanwise locations were used for the HFO where only 5 spanwise locations were used for the LFO.

The multipoint FUN3D optimization followed a similar form as the previously discussed LFO where both the hover and cruise operating conditions detailed in Table 1 were considered at each optimization cycle. It should be noted that unsteady simulations for each operating point were conducted over 5 revolutions prior to optimization for aerodynamic convergence. At each optimization cycle, both operating points were simulated for a full rotor revolution and the cost function and constraints, shown in Table 4, were averaged over the last quarter of a revolution. The cost function and constraints for this portion of the work took a sightly different form than for the LFO shown in Table 2. Rather than the cost function dependency on FM and η, the HFO minimized the torque, Q, at both operating conditions:

$$f_{\text{cost}} = min\{w_h Q_h + w_c Q_c\}, \tag{2}$$

where again, $w_h = 1$ and $w_c = 1$ in this work. The constraint on disk loading effectively maintains the proprotor thrust, meaning that the only free parameter for both FM and η is Q.

Table 4: Cost function and constraints for high-fidelity optimization.

Cost Function	$min\{Q_h + Q_c\}$
DL_h Constraint	7.9 psf $\leq DL_h \leq$ 8.1 psf
DL_c Constraint	1.8 psf $\leq DL_c \leq$ 2.0 psf

RESULTS

Low-Fidelity Optimization

The LFO was allowed a maximum of 2000 iterations. Genetic algorithms, in general, require more iterations than gradient-based optimization problems, and differential evolution, in particular, queries an entire sample space at each iteration, meaning that for 2000 iterations, approximately 705,000 cost function evaluations were performed with a final value of $f_{\text{cost}} = 0.267$, or $FM = 0.830$ and $\eta = 0.904$. The disk loading values corresponding to these performance results were $DL_h = 8.01$ psf and $DL_c = 2.03$ psf, respectively. Final DVs resulting from the LFO are summarized in Table 5. Additionally, the twist and chord length distributions of the proprotor showing both the control points and spline fit are shown in Fig. 7. The distributions of $\alpha(r)$ and the thrust, $T(r)$, per unit span are also shown in Fig. 8 where the black dotted lines in Fig. 8a denote the α limits imposed during the LFO process. As can be seen in Fig. 7, the twist and chord distributions are decreasing outboard of $0.7R$ and have no more than one slope

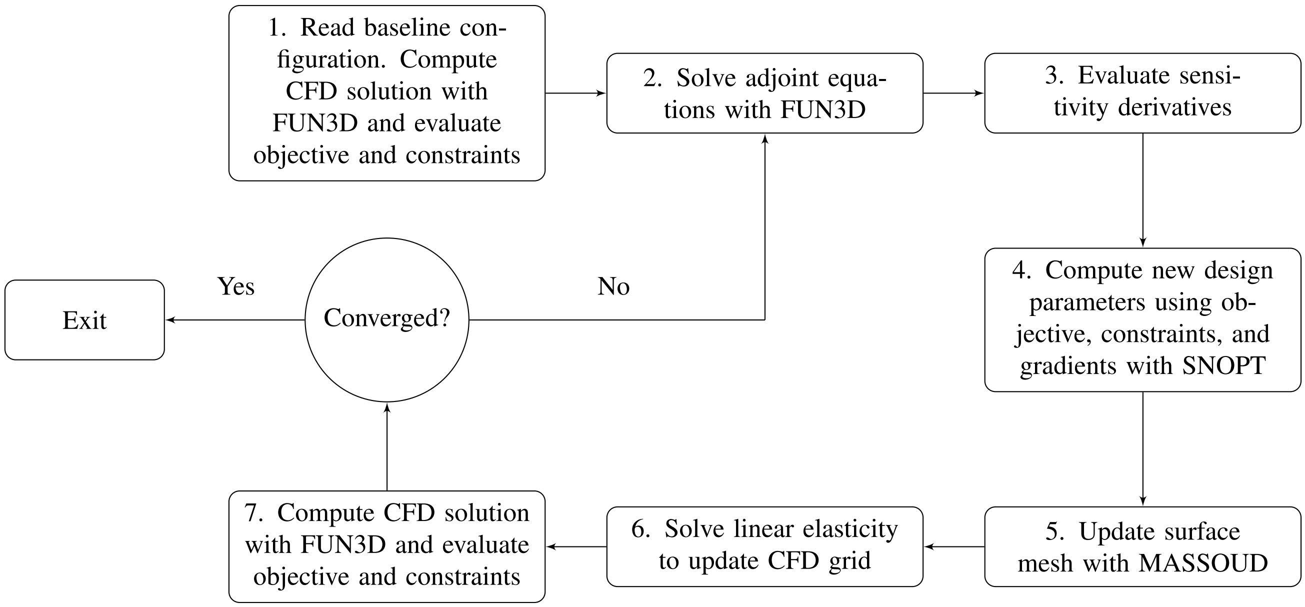

Figure 4: Block diagram representation of high-fidelity gradient-based optimization. Adapted from Wang et al. (Ref. 34).

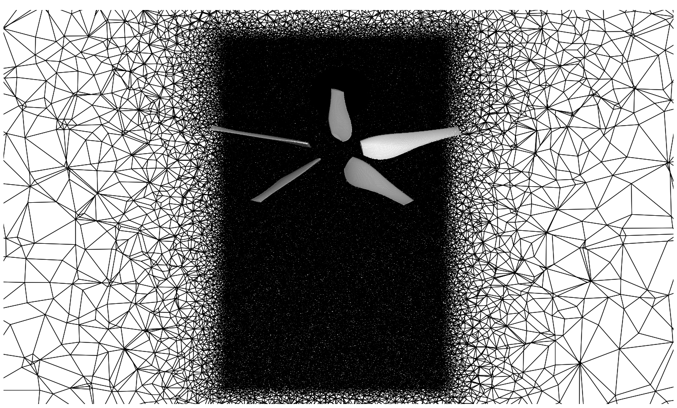

Figure 5: Front view of volumetric grid used for high-fidelity optimization.

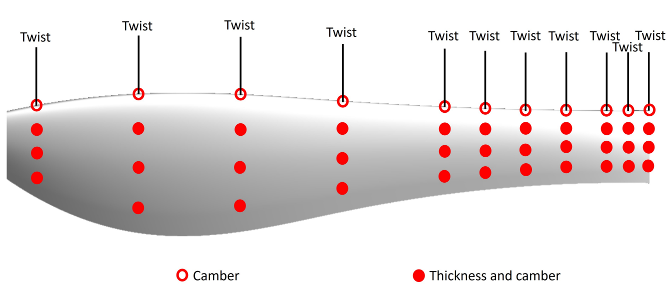

Figure 6: Shape design variables and planform illustration.

change, as prescribed by the constraints listed in Table 2. The $\alpha(r)$ distributions in Fig. 8b can also be seen to adhere to the constraints where all values of $\alpha(r)$ are below stall and above the zero-lift α value. Interestingly, Fig. 8 shows that the proprotor produces an outboard-skewed elliptic-like loading distribution in the hover operating condition. Based on Prandtl's lifting line theory (Ref. 41), the elliptical distribution is thought to achieve minimum induced drag and therefore, optimal efficiency.

Table 5: Design variable results from low-fidelity optimization (1...5 denotes values at the five control points).

Design Variable	Final Value
$\theta_{0,h}$	$-3.970°$
$\theta_{0,c}$	$32.74°$
$\theta_{tw,1}$	$43.93°$
$\theta_{tw,2}$	$33.31°$
$\theta_{tw,3}$	$24.83°$
$\theta_{tw,4}$	$21.11°$
$\theta_{tw,5}$	$9.220°$
c_1	0.3425 ft
c_2	0.7457 ft
c_3	0.5642 ft
c_4	0.3781 ft
c_5	0.3264 ft

Trim and Verification

After successful implementation of the LFO framework, the optimized proprotor was trimmed to the target disk loading values of $DL_h = 8$ psf and $DL_c = 1.9$ psf by adjusting collective pitch using CAMRAD II's free-wake solver. This trimming procedure was performed to establish more accurate operating conditions by considering additional flow physics that were not resolved during the LFO. Following this, the thickness and camber distributions of the proprotor blade were modified for structural robustness and high-fidelity FUN3D simulations were conducted using a fine volumetric spatial resolution and DDES on the modified proprotor for aerodynamic performance verification. A comparison of the aerodynamic performance results is provided in Table 6 for the LFO, mid-fidelity trim, and high-fidelity FUN3D simulations.

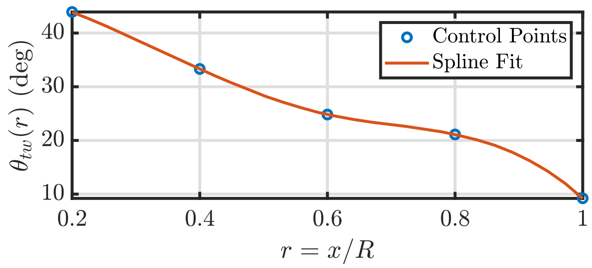

(a) Spanwise twist distribution.

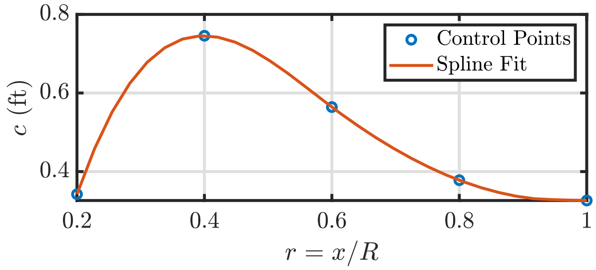

(b) Spanwise chord distribution.

Figure 7: Low-fidelity optimized blade geometric characteristics.

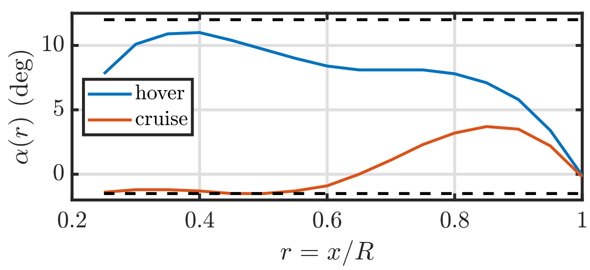

(a) Angle of attack distribution where dashed black lines show optimizer constraints.

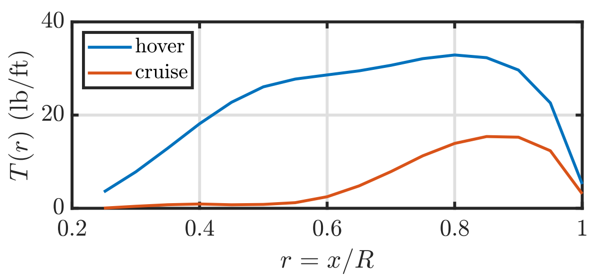

(b) Thrust per unit span distribution.

Figure 8: Low-fidelity optimized blade performance characteristics.

Additionally, a comparison of the thrust distribution, $T(r)$, per unit span between the three methods of varying fidelity is shown in Fig. 9. This figure shows that, although the integrated aerodynamic performance quantities are similar among the three methods, the LFO spanwise loading distribution differs most between the three methods. This can be explained by the absence of a wake model, which leads to a sharper and earlier tip-load roll-off behavior. The mid-fidelity trim aerodynamic solver can be seen to more closely match the trend and behavior of the high-fidelity FUN3D simulation, except for the loading peak near the blade tip observed in the FUN3D simulation. This loading peak near the blade tip is a direct consequence of the tip-vortex formation which is fully resolved by FUN3D but modeled by CAMRAD II's free-wake solver.

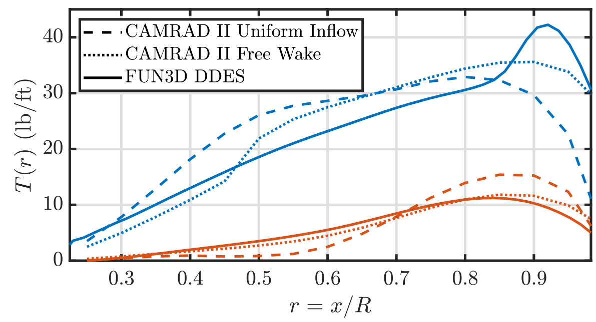

Figure 9: Thrust per unit span comparison between low-fidelity optimization, mid-fidelity trim, and high-fidelity FUN3D verification. Results in blue are for hover and orange for cruise.

High-Fidelity Optimization

The HFO started with the trimmed and modified proprotor discussed in the previous section and was allowed to run for 10 design iterations. The optimizer convergence results for the multipoint cost function, torque in hover and cruise, and ΔDL, or the difference in DL between the target and optimized configurations, are shown in Fig. 10. The dashed black line in Fig. 10c denotes the DL constraint value of $|\Delta DL| < 0.1$. It was observed that DL_h exceeded the imposed DL constraint beyond the fourth iteration and continued to increase after the sixth iteration, as shown in Fig. 10c. Additionally, there was little cost function and torque benefit beyond the sixth iteration, which can be seen in Figs. 10a and 10b. Further study is necessary to determine the cause of this DL_h divergence; however, due to time constraints, the results at the sixth iteration were selected for further discussion, which is indicated by the red dotted line in Fig. 10. The results at iteration six will hereby be denoted as the final results. A summary between the LFO results and the final HFO results at iteration six are given in Table 7.

Interestingly, it can be seen that FM improved by 0.012 while η worsened by 0.012 between the LFO and final HFO results. Though these performance metrics changed only slightly throughout the optimization, Q_c improved drastically by approximately 75 ft-lb. To highlight the torque improvements, the thrust and torque per unit span distributions along the blade span are compared between the LFO and final HFO results in Fig. 11.

It can be seen in Fig. 11a that the thrust distributions remain relatively constant between the LFO and final results, which was expected since the change in DL_h and DL_c was small. The

Table 6: Aerodynamic performance comparison among low-fidelity optimization, mid-fidelity trim, and high-fidelity FUN3D verification. (Note: high-fidelity verification simulated using FUN3D DDES).

Parameter	Low-Fidelity Optimizer	Mid-Fidelity Trim	High-Fidelity Verification
$\theta_{0,h}$	$-3.970°$	$-1.000°$	$-1.000°$
$\theta_{0,c}$	32.74°	33.50°	33.50°
DL_h	8.01 psf	8.19 psf	7.82 psf
DL_c	2.03 psf	1.94 psf	1.93 psf
FM	0.830	0.702	0.714
η	0.904	0.867	0.849

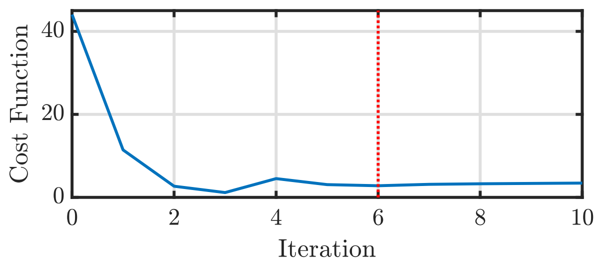

(a) Cost function.

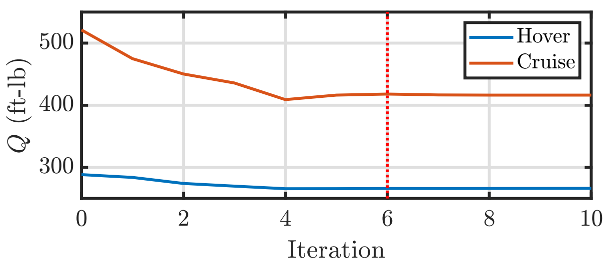

(b) Torque.

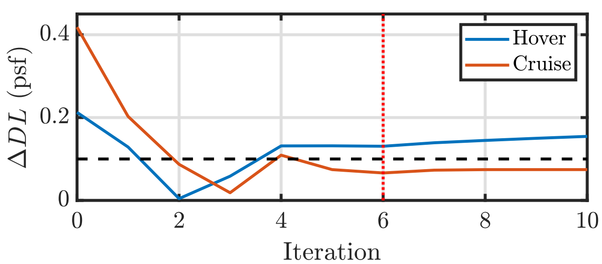

(c) Difference between DL and DL_h or DL_c.

Figure 10: High-fidelity optimization results (Note: beyond iteration six was not used for analysis).

torque distribution can be seen to differ substantially for the cruise operating condition whereas only a small improvement can be seen for the hover operating condition.

Visualizations of the LFO and HFO blade planform and airfoil sections are shown in Figs. 12 and 13, respectively, where the optimized blade is shown in red and the black vertical lines in Fig. 12 indicate slice locations for the airfoil section comparison in Fig. 13. The difference in collective pitch between the LFO and HFO results has been removed from both figures to provided a more direct comparison. It can be seen from Fig. 13 that the blade shape remains nearly unchanged inboard of $0.67R$ with very minor changes outboard of this spanwise location. It is difficult to distinguish any clear trends in the optimized blade shape, though it does appear as though the quarter-chord thickness is increased over most of the blade span, based on the planform comparison in Fig. 12. Additionally, the airfoil section comparison in Fig. 13 shows that there is a thickness reduction aft of the approximate half-chord location outboard of $0.88R$. Based on these negligible

Table 7: High-fidelity optimization results (Note: baseline LFO and final HFO simulated using FUN3D SA).

Parameter	Baseline LFO Value	Final HFO Value
$\theta_{0,h}$	$-1°$	$-2.08°$
$\theta_{0,c}$	33.50°	32.56°
DL_h	8.21 psf	7.87 psf
DL_c	2.32 psf	1.83 psf
Q_h	212.68 ft-lb	196.22 ft-lb
Q_c	384.41 ft-lb	308.32 ft-lb
FM	0.708	0.720
η	0.850	0.839

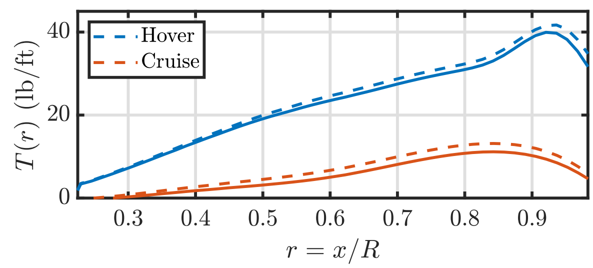

(a) Thrust per unit span distribution.

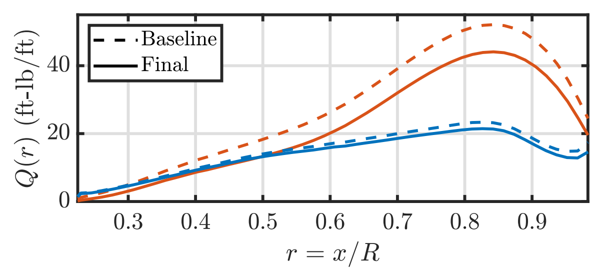

(b) Torque per unit span distribution.

Figure 11: Comparison of aerodynamic thrust and torque distributions between low-fidelity optimization and final high-fidelity optimization results.

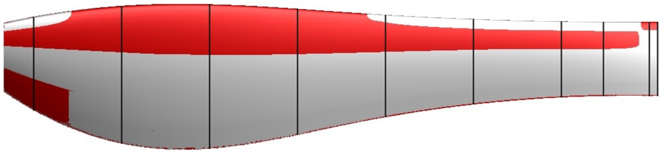

(a) Top view.

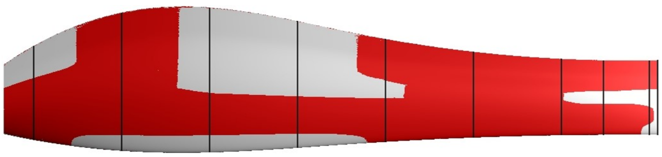

(b) Bottom view.

Figure 12: Visualization of the low-fidelity optimized blade planform in gray and the final high-fidelity optimized blade planform in red (Note: planforms are overlapping).

blade shape differences between the LFO and HFO, it can be said that most of the aerodynamic performance differences between the LFO and HFO shown in Table 7 can be accounted for by changes in collective pitch. These HFO results also suggest that the LFO may have provided a suitable blade design and that the lack of aerodynamic solver fidelity in the LFO was insignificant to the design optimization problem explored in this work.

CONCLUSIONS

A multifidelity multipoint optimization was performed in this work to design a realistic and representative full-sale UAM proprotor to serve as a benchmark research platform for future aerodynamic and acoustic studies. Both hover at sea level standard day and cruise at an altitude of 10,000 ft ISA (i.e., 4000 ft above ground level) operating conditions were considered during the design optimization with a hover and cruise disk loading requirement of 8 psf and 1.9 psf, respectively. The design requirements were derived from Whiteside et al. (Ref. 3) but slightly modified to be characteristic of tilting proprotor-type applications and more representative of recent industry tiltrotor and lift+cruise UAM vehicle designs.

A low-fidelity multipoint optimization was first performed using a differential evolution algorithm. CAMRAD II was used as the aerodynamic solver for this first optimization with a uniform inflow model and no wake modeling. The optimized rotor showed exceptional aerodynamic performance in both the hover and cruise operating conditions with a hover figure of merit of 0.830 and propulsive efficiency in cruise of 0.904. The aerodynamic solver fidelity was then increased and the optimized design was trimmed using CAMRAD II with a nonuniform inflow and free-wake model to establish more accurate operating conditions to be used during a subsequent high-fidelity optimization. The blade root was also adjusted for structural rigidity. Following this mid-fidelity trim and structural modification, high-fidelity CFD using DDES was performed with FUN3D to verify that the changes had negligible impact on aerodynamic performance. Low-, mid-, and high-fidelity results were compared and it was seen that the

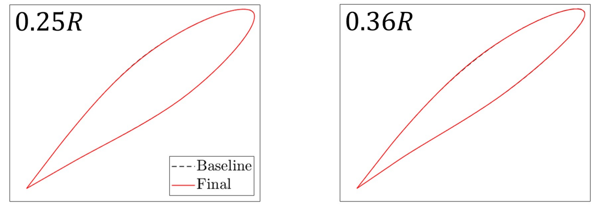

(a) r=0.25R. (b) r=0.36R.

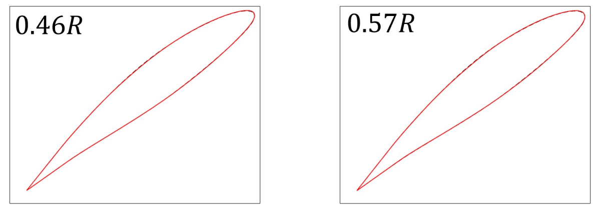

(c) r=0.46R. (d) r=0.57R.

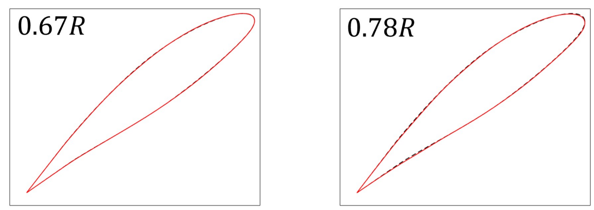

(e) r=0.67R. (f) r=0.78R.

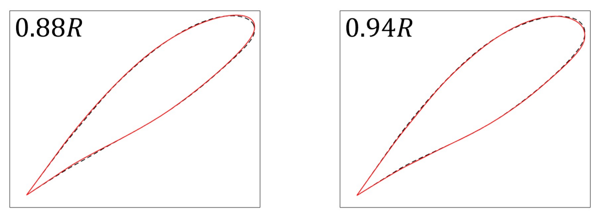

(g) r=0.88R. (h) r=0.94R.

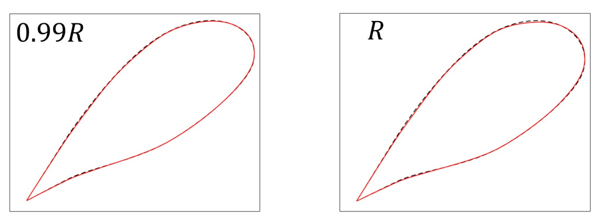

(i) r=0.99R. (j) r=R.

Figure 13: Visualization of the low-fidelity optimized and final high-fidelity optimized airfoil sections (Note: vertical scale exaggerated for clarity).

low-fidelity aerodynamic solver agreed least favorably with the high-fidelity CFD, particularly at the hover operating condition.

Finally, a high-fidelity optimization was performed on the low-fidelity optimized design using FUN3D. This sequential optimization improved the hover figure of merit by 0.012 and worsened the propulsive efficiency in cruise by 0.012, though the torque in cruise was seen to decrease by approximately 75 ft-lb. Minimal blade shape changes were targeted by the high-fidelity optimization with the largest change being the collective pitch in hover and cruise, respectively. Since there was negligible blade shape differences between the low- and high-fidelity optimized blade designs, it is suspected that the low-fidelity solver may have provided a suitable blade design and that the lack of aerodynamic solver fidelity in the low-fidelity optimization may have been insignificant to the design problem explored in this work. Further study toward achieving better high-fidelity design optimization results is warranted and future work may explore the use of free-form deformation boxes. Since the low-fidelity optimized design was verified using high-fidelity CFD to be very aerodynamically efficient, it is suggested that this low-fidelity optimized design be used for future aeroacoustic source noise study.

ACKNOWLEDGMENTS

The authors would like to thank Bill Jones from the Computational Aerosciences Branch at the NASA Langley Research Center for invaluable assistance with blade parameterization. This work was funded by the NASA Revolutionary Vertical Lift Technology (RVLT) project under the Aeronautics Research Mission Directorate (ARMD). Computational resources supporting this work were provided by the Midrange HPC K-Cluster at the NASA Langley Research Center.

REFERENCES

1. Rizzi, S. A., Huff, D. L., Boyd Jr., D. D., Bent, P., Henderson, B. S., Pascioni, K. A., Sargent, D. C., Josephson, D. L., Marsan, M., He, H., and Snider, R., "Urban Air Mobility Noise: Current Practice, Gaps, and Recommendations," Technical Publication NASA/TP-2020-5007433, NASA Langley Research Center, Hampton, VA 23681, USA, October 2020.

2. "eVTOL Aircraft Directory", https://evtol.news/aircraft/ (Acessed September 10, 2024).

3. Whiteside, S. K. S., Pollard, B. P., Antcliff, K. R., Zawodny, N. S., Fei, X., Silva, C., and Medina, G. L., "Design of a Tiltwing Concept Vehicle for Urban Air Mobility," Technical Memorandum NASA/TM-20210017971, NASA Langley Research Center, Hampton, VA 23681, USA, June 2021.

4. Silva, C., Johnson, W., Antcliff, K. R., and Patterson, M. D., "VTOL Urban Air Mobility Concept Vehicles for Technology Development," 2018 Aviation Technology, Integration, and Operations Conference, June 2018. DOI: https://doi.org/10.2514/6.2018-3847

5. Silva, C., and Johnson, W., "Practical Conceptual Design of Quieter Urban VTOL Aircraft," VFS International 77th Annual Forum & Technology Display, May 2021. DOI: https://doi.org/10.4050/F-0077-2021-16739

6. Stoll, A., and Bevirt, J., "Development of eVTOL Aircraft for Urban Air Mobility at Joby Aviation," VFS International 78th Annual Forum & Technology Display, May 2022. DOI: https://doi.org/10.4050/F-0078-2022-17528

7. Tinney, C. E., and Valdez, J. A., "Hover Performance and Acoustics of a 35% Scale Notional eVTOL Rotor," 30th AIAA/CEAS Aeroacoustics Conference, June 2024. DOI: https://doi.org/10.2514/6.2024-3219

8. Fleming, J., Langford, M., Gold, J., Schwartz, K., Wisda, D., Alexander, N., and Whelchel, J., "Measured Acoustic Characteristics of Low Tip Speed eVTOL Rotors in Hover," VFS International 78th Annual Forum & Technology Display, May 2022. DOI: https://doi.org/10.4050/F-0078-2022-17434

9. Pettingill, N. A., Zawodny, N. S., Thurman, C. S., and Lopes, L. V., "Acoustic and Performance Characteristics of an Ideally Twisted Rotor in Hover," AIAA SciTech 2021 Forum, January 2021. DOI: https://doi.org/10.2514/6.2021-1928

10. Thurman, C. S., Zawodny, N. S., Pettingill, N. A., Lopes, L. V., and Baeder, J. D., "Physics-informed Broadband Noise Source Identification and Prediction of an Ideally Twisted Rotor," AIAA SciTech 2021 Forum, January 2021. DOI: https://doi.org/10.2514/6.2021-1925

11. Pettingill, N. A., Zawodny, N. S., and Thurman, C. S., "Aeroacoustic Testing of UAS-Scale Rotors for a Quadcopter in Hover and Forward Flight," 28th AIAA/CEAS Aeroacoustics Conference, June 2022. DOI: https://doi.org/10.2514/6.2022-3110

12. Thurman, C. S., "Computational Study of Boundary Layer Effects on Stochastic Rotor Blade Vortex Shedding Noise," *Aerospace Science and Technology*, Vol. 131A, (107983), 2022. DOI: https://doi.org/10.1016/j.ast.2022.107983

13. Ingraham, D., Gray, J., and Lopes, L. V., "Gradient-Based Propeller Optimization with Acoustic Constraints," AIAA SciTech 2019 Forum, January 2019. DOI: https://doi.org/10.2514/6.2019-1219

14. Abergo, L., Guardone, A., and Gori, G., "Towards a Two-Stage Multi-Fidelity Shape Optimization Approach to Noise Reduction in Urban Air Mobility Applications," 30th AIAA/CEAS Aeroacoustics Conference, June 2024. DOI: https://doi.org/10.2514/6.2024-0245

15. Zawodny, N. S., Pascioni, K. A., and Thurman, C. S., "An Overview of the Proprotor Performance Test in the 14- by 22-Foot Subsonic Tunnel," VFS International 79th Annual Forum & Technology Display,

May 2023. DOI: https://doi.org/10.4050/F-0079-2023-18054

16. Thurman, C. S., Zawodny, N. S., and Pascioni, K. A., "Computational Study of Vortex-Induced Separation for a 5-Bladed Rotor," VFS International 79th Annual Forum & Technology Display, May 2023. DOI: https://doi.org/10.4050/F-0079-2023-17944

17. "Joby Aviation S4 (production prototype)", https://evtol.news/joby-aviation-s4-production-prototype/ (Acessed September 10, 2024).

18. "Archer Aviation", https://archer.com/aircraft/ (Acessed September 10, 2024).

19. "Wisk Aero", https://wisk.aero/aircraft/ (Acessed September 10, 2024).

20. Greenwood, E., Brentner, K. S., Rau, R. F., and Gan, Z. F. T., "Challenges and Opportunities for Low Noise Electric Aircraft," *International Journal of Aeroacoustics*, Vol. 21, (5–7), 2022, pp. 315–381. DOI: https://doi.org/10.1177/1475472X221107377

21. Storn, R., and Price, K., "Differential Evolution - A Simple and Efficient Heuristic for Global Optimization over Continuous Spaces," *Journal of Global Optimization*, Vol. 11, 1997, pp. 341–359. DOI: https://doi.org/10.1023/A:1008202821328

22. Virtanen, P., Gommers, R., Oliphant, T. E., *et al.*, "SciPy 1.0: Fundamental Algorithms for Scientific Computing in Python," *Nature Methods*, Vol. 17, 2020, pp. 261–272. DOI: https://doi.org/10.1038/s41592-019-0686-2

23. Johnson, W., *CAMRAD II: Comprehensive Analytical Model of Rotorcraft Aerodynamics and Dynamics, Vols. I – VII*, Johnson Aeronautics, 2020.

24. Maisel, M. D., Giulianetti, D. J., and Dugan, D. C., "The History of the XV-15 Tilt Rotor Research Aircraft: From Concept to Flight," Book NASA/SP-2000-4517, NASA Office of Policy and Plans, NASA History Division, Washington, DC, USA.

25. Nichols, R. H., Tramel, R. W., and Buning, P. G., "Solver and Turbulence Model Upgrades to OVERFLOW 2 for Unsteady and High-Speed Applications," 24th Applied Aerodynamics Conference, June 2006. DOI: https://doi.org/10.2514/6.2006-2824

26. Tramel, R. W., Nichols, R. H., and Buning, P. G., "Addition of Improved Shock-Capturing Schemes to OVERFLOW 2.1," 19th AIAA Computational Fluid Dynamics Conference, June 2009. DOI: https://doi.org/10.2514/6.2009-3988

27. Anderson, W. K., Biedron, R. T., Carlson, J.-R., Derlaga, J. M., Diskin, B., Druyor Jr., C. T., Gnoffo, P. A., Hammond, D. P., Jacobson, K. E., Jones, W. T., Kleb, B., Lee-Rausch, E. M., Liu, Y., Nastac, G. C., Nielsen, E. J., Padway, E. M., Park, M. A., Rumsey, C. L., Thomas, J. L., Thompson, K. B., Walden, A. C., Wang, L., Wood, S. L., Wood, W. A., and Zhang, X., "FUN3D Manual: 14.0.2," Technical Memorandum NASA/TM-20230004211, NASA Langley Research Center, Hampton, VA 23681, USA, November 2023.

28. Spalart, P. R., Deck, S., Shur, M. L., Squires, K. D., Strelets, M. K., and Travin, A., "A New Version of Detached-eddy Simulation, Resistant to Ambiguous Grid Densities," *Theoretical and Computational Fluid Dynamics*, Vol. 20, 2006, pp. 181–195. DOI: https://doi.org/10.1007/s00162-006-0015-0

29. Spalart, P. R., and Allmaras, S. R., "A One-Equation Turbulence Model for Aerodynamic Flows," 30th AIAA Aerospace Sciences Meeting and Exhibit, January 1992. DOI: https://doi.org/10.2514/6.1992-439

30. Gill, P. E., Murray, W., and Saunders, M. A., "SNOPT: An SQP Algorithm for Large-Scale Constrained Optimization," *SIAM Review*, Vol. 47, (1), 2005, pp. 99–131. DOI: https://doi.org/10.1137/S1052623499350013

31. Samareh, J. A., "Novel Multidisciplinary Shape Parameterization Approach," *Journal of Aircraft*, Vol. 38, (6), 2001, pp. 1015–1024. DOI: https://doi.org/10.2514/2.2888

32. Saad, Y., and Schultz, M. H., "GMRES: A Generalized Minimum Residual Algorithm for Solving Nonsymmetric Linear Systems," *SIAM Journal on Scientific and Statistical Computing*, Vol. 7, (3), 1996, pp. 856–869. DOI: https://doi.org/10.1137/0907058

33. Wang, L., Diskin, B., Biedron, R. T., Nielsen, E. J., and Bauchau, O. A., "High-Fidelity Multidisciplinary Sensitivity Analysis and Design Optimization for Rotorcraft Applications," *AIAA Journal*, Vol. 57, (8), 2019, pp. 3117–3131. DOI: https://doi.org/10.2514/1.J056587

34. Wang, L., Diskin, B., Lopes, L. V., Nielsen, E. J., Lee-Rausch, E. M., and Biedron, R. T., "High-Fidelity Aeroacoustic Optimization Tool for Flexible Rotors," *Journal of the American Helicopter Society*, Vol. 66, (2), 2021, pp. 1–16. DOI: https://doi.org/10.4050/JAHS.66.022004

35. Thurman, C. S., Wang, L., and Padway, E. M., "Broadband Noise Prediction of Two Small Hovering Rotors Using FUN3D-ANOPP2," AIAA SciTech 2025 Forum, January 2025.

36. Roe, P. L., "Approximate Riemann Solvers, Parameter Vectors, and Difference Schemes," *Journal of Computational Physics*, Vol. 43, (2), 1981, pp. 357–372. DOI: https://doi.org/10.1016/0021-9991(81)90128-5

37. Burg, C. O. E., "Higher Order Variable Extrapolation for Unstructured Finite Volume RANS Flow Solvers," 17th AIAA Computational Fluid Dynamics Conference, June 2005. DOI: https://doi.org/10.2514/6.2005-4999

38. Vatsa, V. N., Carpenter, M. H., and Lockard, D. P., "Re-evaluation of an Optimized Second Order Backward Difference (BDF2OPT) Scheme for Unsteady Flow Applications," 48th AIAA Aerospace Sciences Meeting Including the New Horizons Forum and Aerospace Exposition, January 2010. DOI: https://doi.org/10.2514/6.2010-122

39. Noack, R. W., Boger, D. A., Kunz, R. F., and Carrica, P. M., "Suggar++: An Improved General Overset Grid Assembly Capability," 19th AIAA Computational Fluid Dynamics, June 2009. DOI: https://doi.org/10.2514/6.2009-3992

40. Nielsen, E. J., and Diskin, B., "Discrete Adjoint-Based Design for Unsteady Turbulent Flows on Dynamic Overset Unstructured Grids," *AIAA Journal*, Vol. 51, (6), 2013, pp. 1355–1373. DOI: https://doi.org/10.2514/1.J051859

41. Prandtl, L., "Applications of Modern Hydrodynamics to Aeronautics," NACA Report 116, 1923.